POLITECNICO DI TORINO
Repository ISTITUZIONALE

Plasmonic color-graded nanosystems with achromatic subwavelength architectures for light filtering and advanced SERS detection

(Article begins on next page)

26 June 2024

Plasmonic Color-Graded Nanosystems with Achromatic Subwavelength Architectures for Light Filtering and Advanced SERS Detection

Remo Proietti Zaccaria,[†] Francesco Bisio,[*,‡] Gobind Das,[†,§] Giulia Maidecchi,[‖,∇] Michael Caminale,[‖,#] Chinh Duc Vu,[‖,⊥] Francesco De Angelis,[†] Enzo Di Fabrizio,[§] Andrea Toma,[†] and Maurizio Canepa[‖]

[†]Istituto Italiano di Tecnologia, Via Morego 30, 16163 Genova (Italy),

[‡]Istituto Superconduttori, Materiali Innovativi e Dispositivi (SPIN), Consiglio Nazionale delle Ricerche, Corso Perrone 24, 16152 Genova, Italy

[§]PSE Division, King Abdullah University of Science and Technology (KAUST), Thuwal, Saudi Arabia

[‖]OptMatLab, Dipartimento di Fisica, Università degli Studi di Genova, Via Dodecaneso 33, 16146 Genova, Italy

[⊥]Institute of Materials Science, Vietnam Academy of Science and Technology, 18 Hoang Quoc Viet road, Cau Giay District, Hanoi, Vietnam

S *Supporting Information*

ABSTRACT: Plasmonic color-graded systems are devices featuring a spatially variable plasmonic response over their surface. They are widely used as nanoscale color filters; their typical size is small enough to allow integration with miniaturized electronic circuits, paving the way to realize novel nanophotonic devices. Currently, most plasmonic color-graded systems are intrinsically discrete because their chromatic response exploits the tailored plasmon resonance of microarchitectures characterized by different size or geometry for each target color. Here, we report the realization of multifunctional plasmon-graded devices where continuously graded chromatic response is achieved by smoothly tuning the composition of the resonator material while simultaneously maintaining an achromatic nanoscale geometry. The result is a new class of versatile materials: we show their application as plasmonic filters with a potential pixel size smaller than half of the exciting wavelength but also as multiplexed surface-enhanced Raman spectroscopy (SERS) substrates. Many more implementations, such as photovoltaic efficiency boosters or color routers, await and will benefit from the low fabrication cost and intrinsic plasmonic flexibility of the presented systems.

KEYWORDS: plasmonics, color sorting, surface-enhanced Raman spectroscopy, nanoparticles, self-organization
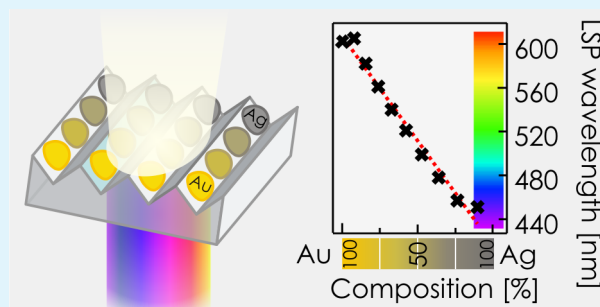
INTRODUCTION

Plasmons are collective resonant oscillations of the free electron gas in metal nanostructures excited by incident electromagnetic (EM) fields;[1−4] they are associated with physical effects of tremendous fundamental and applicative appeal, such as subwavelength manipulation of light and ultrasensitive detection.[5−7]

Plasmon resonances enhance the light-scattering and absorption cross-sections, meaning that well-defined colors may be introduced in nanomaterials by endowing them with tailored metallic resonators supporting plasmons at the desired frequencies. Nanophotonic devices featuring a spatially graded, rather than homogeneous, plasmonic response extend such a color-tailoring concept in a simple, yet extremely appealing, manner. These so-called color-graded plasmonic systems, based on various physical effects and realized by exploiting a number of nanoarchitectures, have indeed recently found exciting new applications in holography, spectral imaging, and color sorting and are becoming an increasingly widespread tool in photonics.[8−19]

When used as color filters, plasmon-graded systems have an obvious advantage over macroscopic optical filters in their intrinsic microscopic size, yet they share the potential disadvantage of being typically tuned to function at a discrete set of wavelengths (analogous to red−green−blue pixels). Thus, albeit the fact that their small size enables the direct integration with downscaled electronics in original hybrid nanophotonic devices, their plasmonic-resonator geometry hardly lends itself to smoothly vary over the microscopic length scales of realistic miniaturized devices to accommodate a truly "continuous" plasmonic grading.
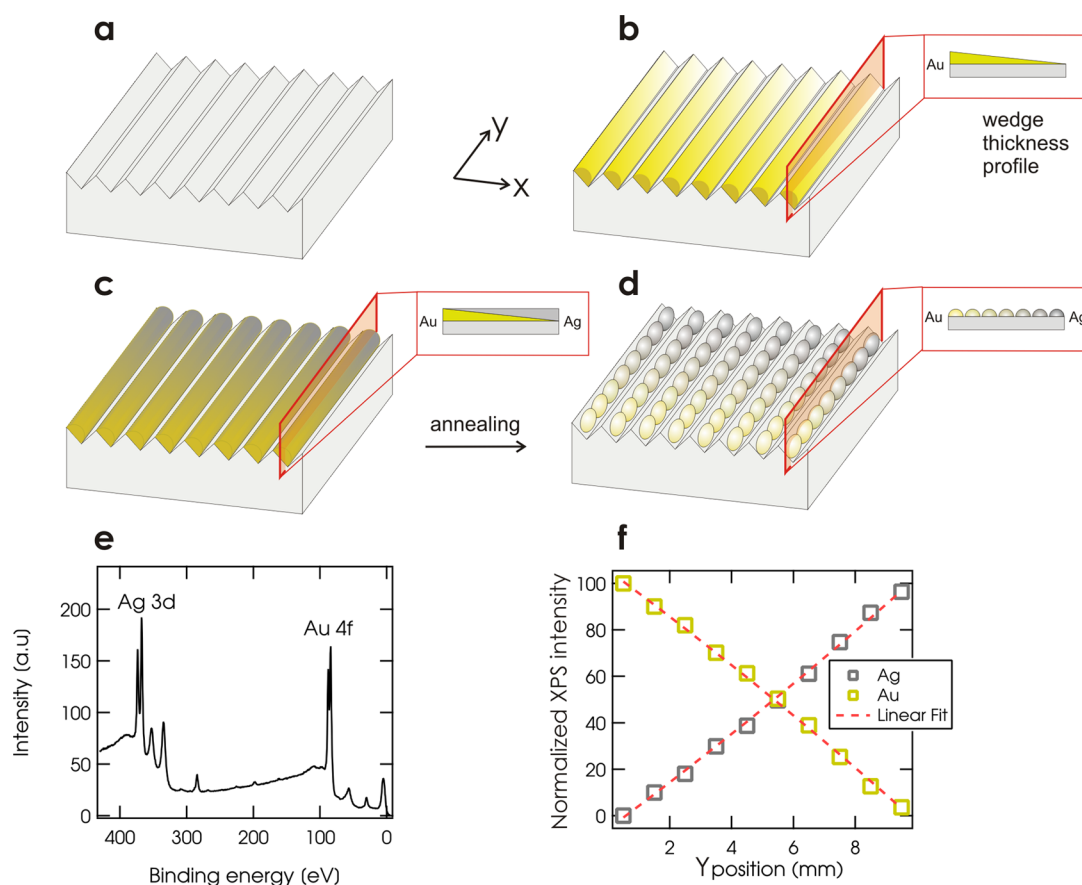
Figure 1. (a−d) Fabrication steps of the color-graded systems. (a) Bare-LiF ridge-valley nanopattern, (b) glancing-angle deposition of Au thickness wedge, (c) glancing-angle deposition of Ag thickness wedge, and (d) annealing at $T = 670$ K. (e) Representative XPS survey spectrum recorded for the $Au_{0.5}Ag_{0.5}$ composition. The Au $4f$ and Ag $3d$ peaks are highlighted. (f) Normalized XPS intensities of Au- and Ag-related XPS signals as a function of the position on the sample.

At variance with these conventional discrete systems, we introduce here the innovative concept of continuously graded plasmonic systems with achromatic subwavelength nano-architectures. We demonstrate a planar plasmonic device where the spatially graded plasmon resonance is a truly continuous function of the spatial coordinates over the sample surface. The plasmonic-color grading is achieved by tuning the chemical composition of the material rather than its geometry, exploiting the plasmon-wavelength tuning of AuAg alloys[20] and thus maintaining a strictly color-invariant nanoscale system architecture.

The devices presented in this paper are composed by two-dimensional (2D) arrays of densely packed $Au_{\alpha}Ag_{(1-\alpha)}$-alloy NPs that continuously span the $0 < \alpha < 1$ composition range over the system surface in a spatially controlled fashion (Figure 1). The mean NP size and the mean interparticle gaps are ∼20 nm and <10 nm, independent of composition, yielding areal NPs density consistently higher than 10^{11} NP/cm^2.

Thanks to the spatially graded composition, the NPs support a localized surface plasmon (LSP) resonance at position-dependent wavelengths spanning the 440−590 nm range when moving from Ag-rich to Au-rich areas over a single device.

This class of materials realizes significant progresses with respect to existing plasmonic color sorters: beside the just-mentioned fine color grading, they allow the further shrinking of the pixel size with respect to existing sorters based on lithographic architectures,[8−19] enabling the integration with smaller-scale devices, while their achromatic geometry enables

an easier integration in photoelectronics. Furthermore, the "achromatic" geometry of chemically graded systems makes them versatile nanophotonics tools: we explicitly demonstrate such a versatility of use for plasmonic filtering applications[8] and advanced plasmon-enhanced Raman spectroscopy (or SERS).[21−23] Many more applications, for broadband photovoltaics (PV) efficiency enhancing,[24] color routing,[13] and more, are at hand simply by engineering the systems microstructure to achieve tailored composition patterns.

■ EXPERIMENTAL SECTION

Sample Fabrication. The systems were fully fabricated in high-vacuum (pressure of $<1 \times 10^{-8}$ mbar) conditions by means of template-driven metal deposition and dewetting.[25,26] First, an insulating nanopatterned substrate was prepared by the homoepitaxial growth of 240 nm of LiF on LiF(110) single crystals (Crystec Gmbh, Berlin, Germany) at $T = 570$ K, leading to a regular ridge-valley surface nanomorphology, where flat crystal facets forming an angle of 45° with the surface normal are formed with periodicity $\Lambda = (27 \pm 5)$ nm (Figure 1a).[27]

Gold and silver were deposited at grazing incidence (60° from the sample normal) by molecular-beam epitaxy at $T = 350$ K (Figure 1b,c) on a 10×10 mm^2 substrate.

The geometrical shadow effect of the ridges leads to the formation of nanowires. A movable mask placed between the evaporator and the sample allowed to obtain thickness wedges of the deposit. Au was deposited first, with equivalent coverage linearly varying as a function of the y coordinate from 0 to 1.7 nm across the sample (Figure 1b). Next, Ag was deposited as a thickness counter-wedge with equivalent
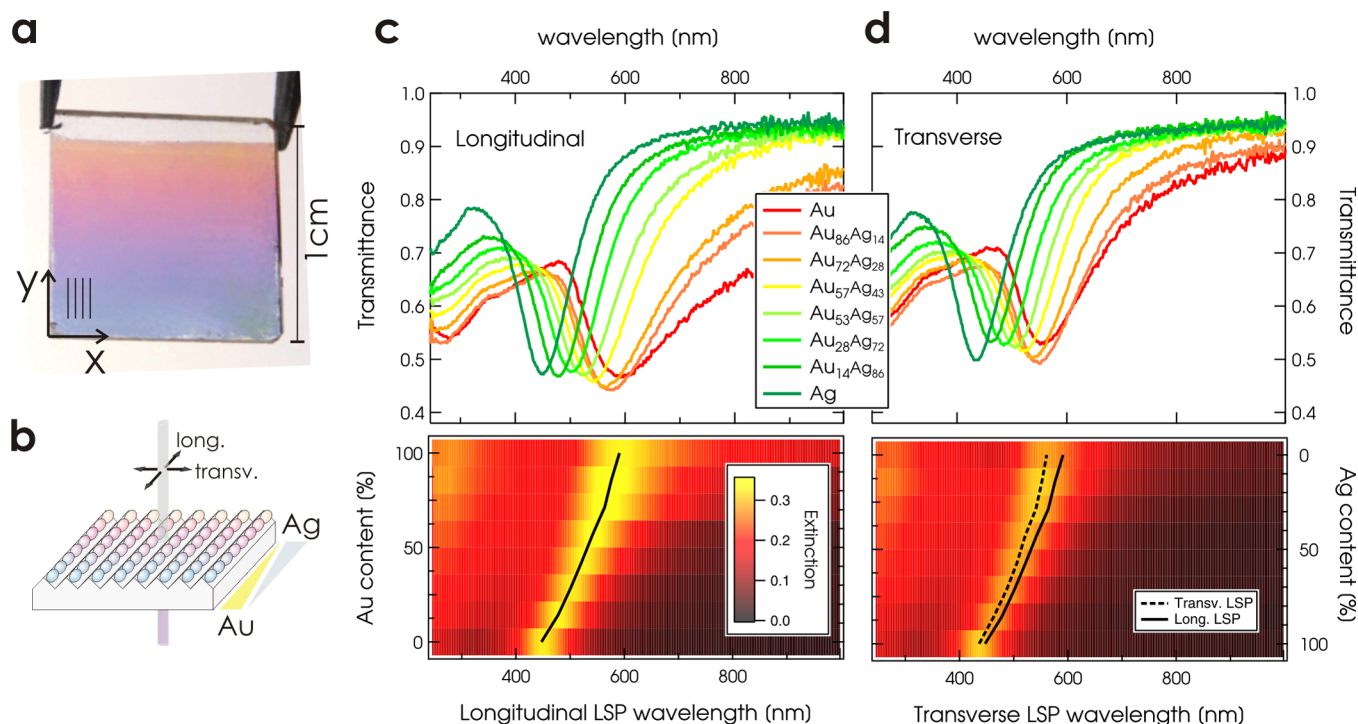
Figure 2. Self-organized Au−Ag alloy nanoparticles arrays. (a) Photograph of a color-graded sample under white-light illumination (1×1 cm^2). Ag-rich (Au-rich) composition are found at the sample top (bottom). Vertical lines show the orientation of nanoridges. (b) Optical geometry employed for the transmission measurements. (c): top, composition-dependent (position-dependent) transmittance spectra in longitudinal configuration. Bottom: corresponding optical-extinction spectra. The longitudinal LSP wavelength vs composition is reported as the continuous black line. (d): top, composition-dependent (position-dependent) transmittance spectra in transverse configuration. Bottom: corresponding optical-extinction spectra. The transverse LSP wavelength vs composition is reported as the dashed black line. For comparison, the longitudinal LSP wavelength is reported as the continuous black line.

coverage from 2.3 nm to 0 (Figure 1c; the uncertainty in metal coverage is around ±5%). In this way, at the top (bottom) edge of the sample the composition of the deposited metal nanowires was pure Ag (Au), and all intermediate mean compositions could be found in between. The bimetallic nanowires were annealed at $T = 670$ K for 20 min in situ to promote their dewetting into regular arrangements of NPs[25,26] (Figure 1d).

Chemical, Optical, and Morphological Characterization. The chemical composition of the samples was measured by X-ray photoelectron spectroscopy (XPS, PHI ESCA 5600 system, with monochromatized Al Kα radiation). In Figure 1e, we report a typical XPS survey spectrum, measured in correspondence of the Au$_{0.5}$Ag$_{0.5}$ composition (after the system annealing), where both Au- and Ag-related features are apparent. From several survey spectra measured in correspondence of different y positions on the sample, we extracted the position-dependent normalized intensity of the most intense peaks (Au 4f and Ag 3d), reported in Figure 1f. The XPS intensity associated with each element varies linearly as a function of the y coordinate.

The optical transmission spectra were measured at normal incidence, with light polarized either parallel (longitudinal geometry) or perpendicular (transverse geometry) to the LiF nanogroove direction (see the scheme in Figure 2b) by means of a J. A.Woollam M-2000X spectrometer (245−1000 nm spectral range). The system morphology was assessed by atomic-force microscopy (AFM, Multimode/Nanoscope IV system, Digital Instruments Veeco).

SERS Measurements. Microprobe Raman measurements were performed by means of Renishaw microRaman spectrometer (model: inVia Raman microscope) in backscattering configuration through a 50× objective. The molecules were excited with two different laser lines, 532 nm (power: 0.035 mW and accumulation time: 15 s) and 633 nm (power: 0.07 mW and accumulation time: 10 s). The system is equipped with a holographic grating of 1800 grooves/mm to acquire the spectral resolution of 1.10 cm^{-1}. Spectral data were analyzed using Renishaw WiRE software 3.0.

■ RESULTS AND DISCUSSION

Plasmonic Subtractive Filtering. The optical response of the system is reported in Figure 2. Figure 2a displays a picture of the sample under white-light illumination. It clearly appears that the graded composition along the y-direction endows the sample with a spatially varying color hue that turns from bluish to yellowish moving from the Au- to the Ag-rich region. The substrate nanogrooves are oriented along the y-direction (parallel to the vertical black lines in the image).

Position-dependent optical transmission spectra in longitudinal (transverse) geometry are reported in the top graph of Figure 2c (Figure 2d). The corresponding extinction patterns are shown in the bottom panels. The marked absorption dip is the fingerprint of the LSP excitation. The LSP shifts from ∼435 nm to nearly 600 nm from the Ag- to the Au-rich region and consists of a single sharp peak for all compositions. At fixed composition, the LSP is narrower and blue-shifted for transverse excitation rather than for longitudinal due to the system uniaxial symmetry. This effect becomes more marked as the composition gets richer in Au as a consequence of the elongation of the Au NPs along the LiF ridge direction.[25] The LSP wavelength can be well-approximated by a linear function of the Au (Ag) content (black lines in Figure 2c,d).

In Figure 3, we report an analysis of the system morphology spanning the whole composition range. Figure 3a shows a set of slices from representative AFM images recorded in correspondence of increasing Ag content (from left to right). The images show regularly arranged NPs laid in the form of closely spaced linear chains corresponding to the underlying LiF nanogrooves.
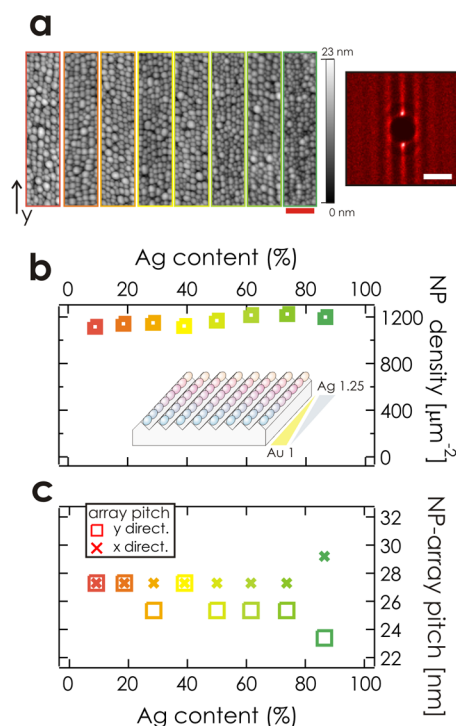
Figure 3. Morphology of the NP array vs NP composition. (a) AFM images of the 2D NP array at different locations on the same sample, corresponding to nanoparticles with different relative Au (Ag) content (image size: 160×720 nm^2, scale bar: 150 nm). The Au (Ag) percentage corresponds to the one reported in panels b and c for the marker color corresponding to the image-edge color. Right panel: 2D autocorrelation of the relative NP position (autocorrelation area: 200×200 nm^2, scale bar: 50 nm). Bright (dark) areas represent higher (lower) probability for a NP to be found at a certain position with respect to a given particle (see text for details). (b) NP density as a function of composition, deduced from the AFM images of panel a. (c) Mean NP-array pitch along (squares) and across (crosses) the LiF nanoridges as a function of the relative Ag content.

A qualitative inspection already reveals that the morphology stays remarkably invariant independent of material composition, undoubtedly one of the most striking properties of the system. This suggests an intrinsically robust and material-independent process of dewetting and aggregation of the AuAg nanowires during their irreversible temperature-driven evolution toward NPs. The substrate grooves are crucial in this process, providing constraints for atomic mobility and effectively narrowing the accessible system configurations helping to achieve composition-independent morphology. The achromatic characteristics of the NP arrays are confirmed by a quantitative analysis performed by digital NP recognition that yielded the NP spatial density and allowed us to calculate the 2D autocorrelation of NP position (Figure 3a, right). The recognition algorithm "isolates" each particle and determines the position of its center. The 2D spatial autocorrelation is obtained by counting how many particles are found having their center at a certain relative position with respect to every other given particle. Thus, the very bright spots around the image center show strong nearest-neighbor order for NPs in the array, allowing the deduction of the mean array pitch along and across the LiF ridge direction. The mean NP density, reported in Figure 3b, lies around $1.15 \cdot 10^{11}$ NP/cm^2 with *relative variations of less than $\pm 5\%$ throughout the whole composition range*. The mean array pitch along the y- and the x-directions, reported in

Figure 3c (squares and crosses, respectively), is around (26 ± 3) nm and (27 ± 2) nm, with only minor deviations over the whole composition.

Because we know the thickness t of the deposited Au (Ag) from the evaporators calibration and the NP areal density ρ from the AFM images, it is straightforward to calculate the mean NP volume, as $V = t/\rho$. The mean NP volume was 1450 nm^3 (Au), 1730 nm^3 (Au$_{0.5}$Ag$_{0.5}$), and 2000 nm^3 (Ag) and intermediate values for compositions in between. Approximating the NP shape (independent of composition because particle are formed based on the same physical effect), as hemispheres lying on the nanofacets of the rippled LiF surface, we obtain a mean NP diameter of 17.5 (Au), 19 (Au$_{0.5}$Ag$_{0.5}$), and 20 nm (Ag). The mean interparticle gaps along the nanogrooves can be deduced subtracting the NP diameter from the NP-array pitch along the y direction, yielding mean values well below 10 nm. High-resolution scanning-electron-microscopy images agree with these values, though severe charging prevented a more precise estimation.

Combining all the above data, we can also achieve a good estimation of the NP composition. The optical data, showing a single LSP peak linearly shifting in wavelength versus the NP nominal composition, strongly suggest the formation of a homogeneous alloy for all the compositions.[20,28] This assumption is reinforced by the position dependence of the XPS intensity of Au and Ag peaks (Figure 1e). The surface sensitivity of XPS implies indeed that only the few outermost nanometers from the NP surface are probed. Thus, the linear trend of XPS intensity versus nominal Au (Ag) composition is a clear indication that no surface enrichment of any of the two metals has occurred, ruling out core–shell, Janus, or other complex morphologies.

Plasmon-Enhanced SERS. Although the above data indicate the achievement of continuously graded color filtering, the major novelty of our chemically graded systems is that they represent a new class of versatile materials not limited in application to plasmon-filtering but exploitable for many more nanophotonics applications. One of the most striking, and one that exploits the very same fabrication procedure as just described, is plasmon-graded SERS.

Indeed, the system geometry is such to exhibit plentiful electric-field hot spots, crucial for SERS, and although the density *and* geometry of these hot spots stay independent of composition, the composition grading simultaneously allows the LSP to vary position-wise. Thus, this variable LSP substrate enables the ability to spatially tune the spectral overlap between the SERS excitation source, the substrate LSP, and any eventual molecular resonance while at the same time preserving a strictly identical nanomorphology, something that conventional color sorters cannot guarantee. The combination of these features therefore transforms our plasmon-graded media into hyper-substrates that may significantly innovate with respect to "monochromatic" SERS platforms.

As a proof-of-principle, we therefore performed SERS experiments on our chemically graded samples targeting 4-mercaptobenzoic acid (4-MBA), a molecule specifically chosen for its nonresonant behavior across the LSP range of interest.[29] For such a molecule, the color-graded SERS provides an undistorted mapping of the electric-field enhancement ratio all over the composition range, a relevant quantity that was directly compared with theoretical calculations, thus unambiguously proving the origin of the effect.

For the SERS experiments, 4-mercaptobenzoic acid (Sigma-Aldrich, 99% purity) was deposited from a 1 μM ethanol solution over the device immediately after its removal from the high-vacuum vessel (to keep environmental contamination to a minimum), left in incubation for 12 h, and then rinsed in pure ethanol and dried under a nitrogen flux.

Following the molecule chemisorption, the system preserved its plasmon grading, with a LSP red shift arising from the self-assembled molecular-layer formation on the exposed NP surface.[30] In Figure 4a, the composition-dependent longitudinal
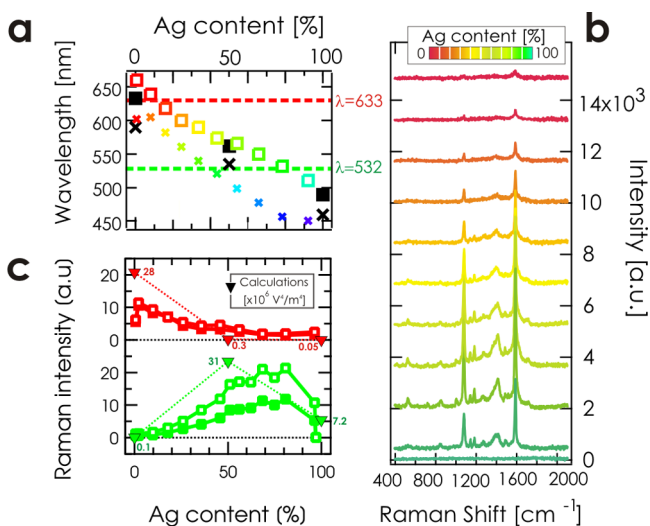

Figure 4. (a) Longitudinal LSP vs composition for the nude (crosses) and dressed (open squares) NPs. Experimental data (colored markers) are compared to calculated values (black markers). The horizontal red (green) line marks the λ = 633 nm (λ = 532 nm) exciting-laser wavelength. (b) SERS spectra of 4-MBA measured with 532 nm excitation as a function of NP composition. The color code of each spectrum corresponds to the composition via the palette in the topmost part of the graph. (c) Normalized SERS intensity of the 1587 cm^{-1} (open markers) and 1076 cm^{-1} (solid markers) SERS peaks as a function of composition for 4-MBA. Green (red) curve: data measured with 532 nm (633 nm) laser excitation. The triangular markers correspond to the calculated Raman intensity according to the near-field calculations reported in Figure 5.

LSP wavelength of the pristine system (colored crosses, henceforth defined as "nude particles") and following the 4-MBA deposition (colored open squares, "dressed particles") is reported. A red shift is clearly observed after the deposition of 4-MBA molecule (Figure 4a). After exciting the system with either 532 or 633 nm lasers, it is apparent that the excitation wavelengths (green, red horizontal dashed lines in Figure 4a) may overlap the substrate LSP wavelength at different spots, (i.e., at specific Au−Ag alloy compositions) on the chemically graded substrate.

The composition-dependent SERS spectra of 4-MBA molecules excited with a 532 nm laser are reported in Figure 4b (top to bottom, Au-rich to Ag-rich regions) exhibiting vibrational bands characteristic of 4-MBA.[31] The SERS intensities have been normalized to the respective areas of the S 2p-orbital contribution, as measured in XPS (not shown), assumed proportional to the 4-MBA chemisorbed on the sample (experimentally almost constant versus composition).

In general, the SERS signals under each laser vary with the degree of spectral overlap between the LSP and the excitation wavelength (green and red horizontal lines in Figure 4a), being

this the main factor that governs the electric-field enhancement ratio. This is shown in Figure 4b with 532 nm excitation: the SERS intensity starts very low on the pure-Au side (out of plasmon resonance), sharply increases upon approaching the Ag-rich area (plasmon-resonant region), and then drops toward the pure-Ag end (out-of-resonance), maintaining an invariant peak shape.

The SERS intensity versus composition of the vibrational bands centered at 1587 and 1076 cm^{-1} is plotted in Figure 4c (full and open squares, respectively). The green symbols represent the SERS intensity with 532 nm excitation, while the red symbols are the output of analogous measurements with a 633 nm laser. The 633 nm yield monotonously increases moving from the Ag-rich to the Au-rich areas.

The spectral overlap between the excitation source and the LSP, and hence the SERS yield, are therefore smoothly tunable simply by scanning the excitation-laser over different spots *on the same substrate*. Thus, any resonance or off-resonance condition is freely achievable on the very same system, and even in cases where the substrate LSP is significantly red-shifted by the target molecule, the resonance matching condition can be re-established simply by a proper shift of the laser spot. We believe the most interesting application may be found addressing resonance Raman effects[32,33] in aptly chosen molecules. LSP-graded substrates might in this case provide superior performances with respect to conventional platforms, allowing more freedom in matching the spectral overlap between the sources of resonance.

Theoretical Simulations. To quantitatively estimate the electric-field enhancement ratio, we performed optical simulations through a numerical tool based on the Finite Integration Technique (FIT) method (CST Microwave Studio) with the purpose of comparing the experimental and theoretical SERS yields.[34] We employed FIT to determine near- and far-field optical responses (electric-field enhancements and the extinction spectra) associated with three material configurations Au, $Au_{0.5}Ag_{0.5}$, and Ag. Convergence analysis was performed to guarantee an error below 5% on the near-field calculations and less than 1% for the far-field results.

To model the optical properties of Au and Ag nanoparticles, we considered the Drude−Lorentz description as in ref 35. However, for the $Au_{0.5}Ag_{0.5}$ alloy, we performed experimental analysis of the material permittivity, and the results were imported in the numerical tool. In all cases, a semi-infinite LiF ($n \approx 1.39$) substrate in the z-direction was considered.

We have modeled the NPs as hemispheres laid on the nanogroove facet facing the deposition source, assuming periodic boundary conditions for the simulation unit cell, with corresponding (x, y) periods deduced from the experimental data. Only a single unit cell is reported in the figures for the sake of clarity, but the system is periodic in the x and in the y direction. Similarly, the nanoparticle cores (no coating) were chosen as 9 nm for Au, 9.5 nm for $Au_{0.5}Ag_{0.5}$, and 10 nm for Ag. The calculations were performed for particles in nude configuration or coated with a 3 nm thick dielectric layer (n = 1.45) to simulate the 4-MBA coating (dressed) in agreement with the experimental LSP red shift upon 4-MBA deposition. The 3 nm layer is larger than the molecule dimensions, possibly due to the presence of physisorbed molecules.[36−39] The amplitude of the electric field associated with the incident plane wave was taken equal to 1 V/m in vacuum, and the EM field was polarized along the NP chains. Far-field extinction spectra were calculated first, and following a
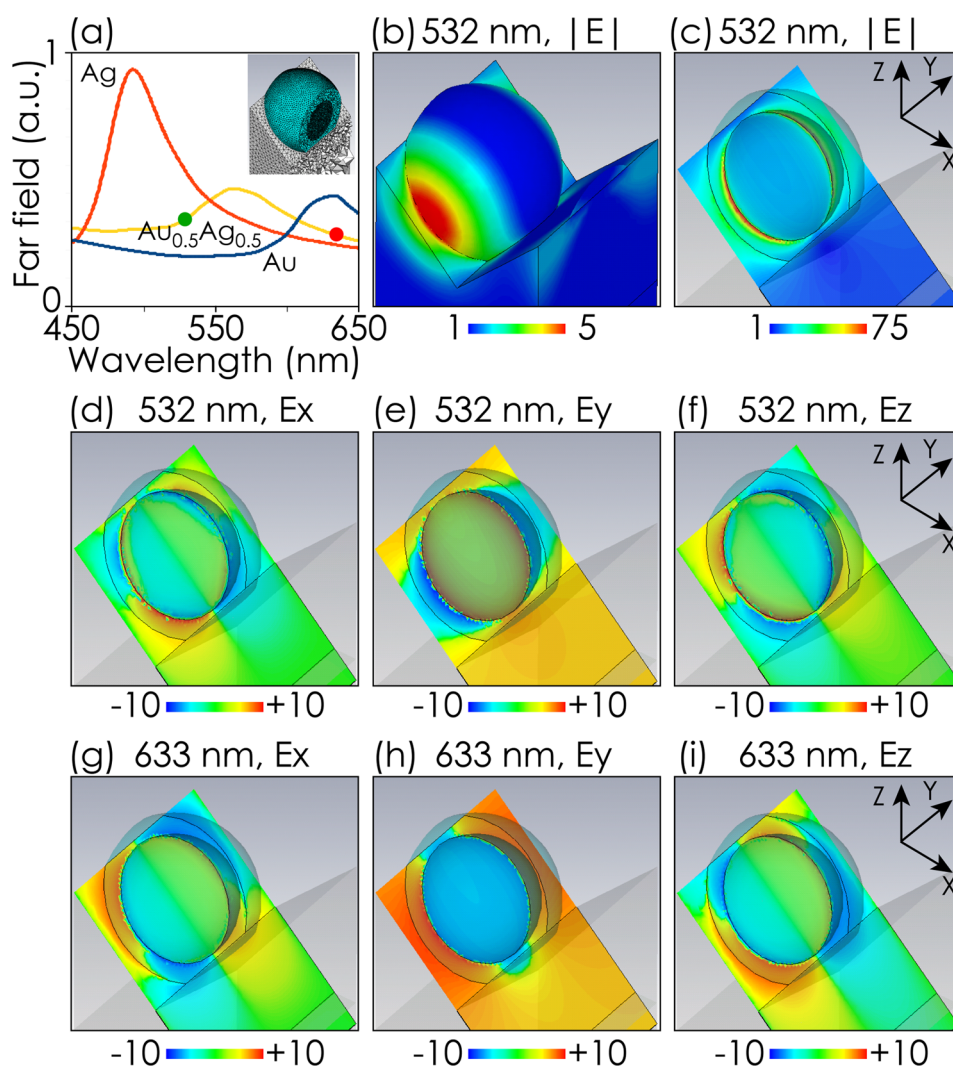
Figure 5. (a) Extinction spectra for the three material configurations when a 3 nm layer of 4-mercaptobenzoic acid is deposited on the nanoparticles. The green (red) dot corresponds to 532 nm (633 nm). The inset shows the mesh resolution (mesh <0.5 nm). (b−i) Near-field maps calculated for $Au_{0.5}Ag_{0.5}$. (b,c) Electric-field enhancements for the 532 nm excitation calculated immediately outside the 4MBA layer and the metallic nanoparticle, respectively. Both the directionality of the field and its strong decay are clearly visible. (d−f) Components of the electric field at 532 nm. (g−i) Components of the electric field at 633 nm.

successful comparison with experimental data, the corresponding near-field maps were simulated.

In Figure 4a, the calculated far-field LSP wavelength for nude and dressed NPs (black crosses and squares) are compared with the experimental data. In both cases, the simulations well-reproduce the experimental results, suggesting the substantial adherence of the simulated geometry with the experimental one despite the necessary simplifications. In detail, we found that in closely packed 2D NP arrays, the dipolar LSPR has a weak dependence on the NP shape, thus justifying in retrospect the choice of a simple NP geometry such as the hemispherical shape (see refs 26 and 40 for a more detailed discussion of the impact of geometrical approximations on the simulated spectra).

The full far- and near-field optical simulation results are reported in Figure 5. Figure 5a displays the extinction spectra for the three material compositions in the dressed configuration and the mesh employed for the calculations. The maxima of the plots correspond to the black square symbols in Figure 4a. Figure 5b−i describes the electric field distribution for the case of the $Au_{0.5}Ag_{0.5}$ alloy (the maps for the pure-Ag and pure-Au

cases are shown in Figure S1 and S2). Panels b and c of Figure 5 show that strong EM-field enhancement occurs indeed within the NP gaps and that the LSP mode strongly decays from the metallic core into the 4-MBA layer, respectively. The maximum field-enhancement ratio for dressed Au, $Au_{0.5}Ag_{0.5}$, and Ag NPs reads approximately 18, 75, and 52 for 532 nm excitation (73, 23, and 15 for 633 nm). Figure 5d−f (Figure 5g−i) shows the Cartesian components of the electric field for the 532 nm (633 nm) excitation. Interestingly, the components associated with 532 and 633 nm are shifted by $\lambda/2$ with respect to each other due to the different relative position of these wavelengths with respect to the LSP maximum (Figure 4a, green dot for 532 nm and red dot for 633 nm[41]).

To deduce the theoretical trend of SERS yield from the calculations, we have estimated the maximum electric-field enhancement at the LiF−air interface in proximity of the metallic nanoparticle and reported the fourth power of the calculated amplitude field in the graph of Figure 4c (triangles). The experimental and numerical results are in good agreement, confirming that the plasmon grading is indeed the dominant

effect determining the composition dependence of the SERS intensity.

CONCLUSIONS

Summarizing, we have successfully realized plasmon-graded systems with smoothly varying LSP resonance and color-independent nanomorphology, acting as plasmonic subtractive filters with a remarkable color-independent extinction. Beside their great ease of fabrication, these systems bring significant advantages with respect to structurally colored plasmon filters. First, they do not require a priori choice of discrete plasmon-wavelength sets but exhibit a smooth LSP shift versus the spatial coordinates. Second, their intrinsic "pixel size" (i.e., the minimum surface area required to establish plasmonic response) can be smaller than other plasmonic filters. Considering that each NP sits on a ~30 × 30 nm^2 area and that LSP characteristics in finite NP chains saturate for 6−7 aligned particles,[42] pixels with <200 nm linear dimensions become readily accessible, smaller than $\lambda/2$ over the whole spectral range. This value can further shrink at the expense of a slight LSP spectral broadening. The subwavelength pixel size cannot be exploited in far-field applications, yet it allows the excitation with subwavelength resolution of materials coupled in the near-field regime with the NP arrays. Small changes in the metal coverage or the annealing procedures lead indeed to different optical responses,[25] endowing the systems with an intrinsic flexibility.

Keeping Au and Ag as the plasmonic materials, the LSP-wavelength range is presently limited to 435−600 nm, a value that can be slightly stretched by a clever tuning of the absolute Au and Ag coverage on the sample to 430−610 nm (nude particles). Strategies to cover the whole visible range can be a thickness-graded dielectric coating or the introduction of materials other than Au or Ag. Aluminum could be a viable option for extending to lower wavelengths, but issues of alloying and material reactivity should be addressed.[40]

Our chemically graded color sorters represent a significant advance in nanophotonics mainly thanks to their versatility of use: they have the potential of acting either as plasmonic subtractive filters, advanced SERS substrates, plasmonic lenses, broadband photovoltaic enhancers, and more. In this work, we explicitly demonstrate their functionality as plasmon filters and SERS substrates (i.e., the applications that required the least sophisticated fabrication schemes). Indeed, whereas we addressed systems realized by bottom-up fabrication, we feel that chemically graded systems with an even higher degree of control can be realized also by lithographic methods and have a significant impact in plasmon-enhanced PV, spectral filtering, or color routing. Speaking of spectral filtering, it can be possible by lithography to define a proper deposition mask to realize color filter arrays of various types (e.g., Bayer). In PV applications, the composition grading can be engineered over the surface of a PV cell so that radiation scattering within the active layer can occur over a broader spectral range than conventional systems, allowing for better overall efficiency enhancement. Analogously, for color routing, composition-graded systems with tailored gradients and spatial extents can allow the flexible extension of the simple approach of bimetallic nanoantennas,[13] possibly leading to sophisticated plasmon routers with a high degree of control over light focusing or directing.

ASSOCIATED CONTENT

Supporting Information

The Supporting Information is available free of charge on the ACS Publications website at DOI: 10.1021/acsami.6b00726.

Figures showing calculated extinction spectra and near-field maps for the pure Ag and pure Au configurations; dielectric functions of Au, Ag, and Au$_{0.5}$Ag$_{0.5}$ used for simulations; and optical properties of NP arrays prior to and after the deposition of 4MBA. (PDF)

AUTHOR INFORMATION

Corresponding Author

*Tel: +39 010 3536287; fax: +39 010 314218; e-mail: francesco.bisio@spin.cnr.it.

Present Addresses

#INAC-SPINTEC, CEA, 17 rue des Martyrs - Bat. 10.05, F-38000 Grenoble, France.
∇Istituto Italiano di Tecnologia, Via Morego 30, 16163 Genova, Italy

Author Contributions

The manuscript was written through contributions of all authors. All authors have given approval to the final version of the manuscript.

Notes

The authors declare no competing financial interest.

REFERENCES

(1) Kreibig, U.; Genzel, L. Optical Absorption of Small Metallic Particles. *Surf. Sci.* **1985**, *156*, 678−700.

(2) Barnes, W. L.; Dereux, A.; Ebbesen, T. W. Surface plasmon subwavelength optics. *Nature* **2003**, *424*, 824−830.

(3) Schuller, J. A.; Barnard, E. S.; Cai; Wenshan, J.; Jun, Y. C.; White, J. S.; Brongersma, M. L. Plasmonics for Extreme Light Concentration and Manipulation. *Nat. Mater.* **2010**, *9*, 193−204.

(4) Maier, S. A. *Plasmonics: Fundamentals and Applications*; Springer: New York, 2007.

(5) Maier, S. A.; Kik, P. G.; Atwater, H. A.; Meltzer, S.; Harel, E.; Koel, B. E.; Requicha, A. A. G. Local Detection of Electromagnetic Energy Transport Below the Diffraction Limit in Metal Nanoparticle Plasmon Waveguides. *Nat. Mater.* **2003**, *2*, 229−232.

(6) Anker, J. N.; Hall, W. P.; Lyandres, O.; Shah, N. C.; Zhao, J.; Van Duyne, R. P. Biosensing with Plasmonic Nanosensors. *Nat. Mater.* **2008**, *7*, 442−453.

(7) Giugni, A.; Torre, B.; Toma, A.; Francardi, M.; Malerba, M.; Alabastri, A.; Proietti Zaccaria, R.; Stockman, M. I.; Di Fabrizio, E. Hot-Electron Nanoscopy Using Adiabatic Compression of Surface Plasmons. *Nat. Nanotechnol.* **2013**, *8*, 845−852.

(8) Zeng, B.; Gao, Y.; Bartoli, F. Ultrathin Nanostructured Metals for Highly Transmissive Plasmonic Subtractive Color Filters. *Sci. Rep.* **2013**, *3*, 2840.

(9) Xu, T.; Wu, Y.-K.; Luo, X.; Guo, L. J. Plasmonic Nanoresonators for High-Resolution Colour Filtering and Spectral Imaging. *Nat. Commun.* **2010**, *1*, 59.

(10) Laux, E.; Genet, C.; Skauli, T.; Ebbesen, T. W. Plasmonic Photon Sorters for Spectral and Polarimetric Imaging. *Nat. Photonics* **2008**, *2*, 161−164.

(11) Do, Y. S.; Park, J. H.; Hwang, B. Y.; Lee, S.-M.; Ju, B.-K.; Choi, K. C. Plasmonic Color Filter and its Fabrication for Large-Area Applications. *Adv. Opt. Mater.* **2013**, *1*, 133−138.

(12) Yokogawa, S.; Burgos, S. P.; Atwater, H. A. Plasmonic Color Filters for CMOS Image Sensor Applications. *Nano Lett.* **2012**, *12*, 4349−4354.

(13) Shegai, T.; Chen, S.; Miljkovic, V. D.; Zengin, G.; Johansson, P.; Käll, M. A Bimetallic Nanoantenna for Directional Colour Routing. *Nat. Commun.* **2011**, *2*, 481.

(14) Ozaki, M.; Kato, J.; Kawata, S. Surface-Plasmon Holography with White-Light Illumination. *Science* **2011**, *332*, 218−220.

(15) Wu, Y.-K. R.; Hollowell, A. E.; Zhang, C.; Guo, L. J. Angle-Insensitive Structural Colours based on Metallic Nanocavities and Coloured Pixels beyond the Diffraction Limit. *Sci. Rep.* **2013**, *3*, 1194.

(16) Zhang, X.; Ye, S.; Zhang, X.; Li, Z.; Wu, S.; Zhang, J.; Wang, T.; Yang, B. Panchromatic Plasmonic Color Patterns: from Embedded Ag Nanohole Arrays to Elevated Ag Nanohole Arrays. *J. Mater. Chem. C* **2013**, *1*, 933−940.

(17) Zhang, Z.; Weber-Bargioni, A.; Wu, S. W.; Dhuey, S.; Cabrini, S.; Schuck, P. J. Manipulating Nanoscale Light Fields with the Asymmetric Bowtie Nano-Colorsorter. *Nano Lett.* **2009**, *9*, 4505−4509.

(18) Kumar, K.; Duan, H.; Hegde, R. S.; Koh, S. C. W.; Wei, J. N.; Yang, J. K. W. Printing Colour at the Optical Diffraction Limit. *Nat. Nanotechnol.* **2012**, *7*, 557−561.

(19) Xu, T.; Wu, Y.-K.; Luo, X.; Guo, L. J. Plasmonic Nanoresonators for High-Resolution Colour Filtering and Spectral Imaging. *Nat. Commun.* **2010**, *1*, 59.

(20) Link, S.; Wang, Z. L.; El-Sayed, M. A. Alloy Formation of Gold Silver Nanoparticles and the Dependence of the Plasmon Absorption on Their Composition. *J. Phys. Chem. B* **1999**, *103*, 3529−3533.

(21) Chirumamilla, M.; Toma, A.; Gopalakrishnan, A.; Das, G.; Zaccaria, R. P.; Krahne, R.; Rondanina, E.; Leoncini, M.; Liberale, C.; De Angelis, F.; Di Fabrizio, E. 3D Nanostar Dimers with a Sub-10-nm gap for Single-/Few-Molecule Surface-Enhanced Raman Scattering. *Adv. Mater.* **2014**, *26*, 2353−2358.

(22) Das, G.; Chirumamilla, M.; Toma, A.; Gopalakrishnan, A.; Zaccaria, R. P.; Alabastri, A.; Di Fabrizio, E.; Leoncini, M. Plasmon Based Biosensor for Distinguishing Different Peptides Mutation States. *Sci. Rep.* **2013**, *3*, 1792.

(23) D'Andrea, C.; Bochterle, J.; Toma, A.; Huck, C.; Neubrech, F.; Messina, E.; Fazio, B.; Maragò, O. M.; Di Fabrizio, E.; Lamy de la Chapelle, M.; Gucciardi, P. G.; Pucci, A. Optical Nanoantennas for Multiband Surface-Enhanced Infrared and Raman Spectroscopy. *ACS Nano* **2013**, *7*, 3522−3531.

(24) Ferry, V. E.; Sweatlock, L. A.; Pacifici, D.; Atwater, H. A. Plasmonic Nanostructure Design for Efficient Light Coupling into Solar Cells. *Nano Lett.* **2008**, *8*, 4391−4397.

(25) Anghinolfi, L.; Moroni, R.; Mattera, L.; Canepa, M.; Bisio, F. Flexible Tuning of Shape and Arrangement of Au Nanoparticles in 2-Dimensional Self-Organized Arrays: Morphology and Plasmonic Response. *J. Phys. Chem. C* **2011**, *115*, 14036−14043.

(26) Maidecchi, G.; Gonella, G.; Proietti Zaccaria, R.; Moroni, R.; Anghinolfi, L.; Giglia, A.; Nannarone, S.; Mattera, L.; Dai, H.-L.; Canepa, M.; Bisio, F. Deep Ultraviolet Plasmon Resonance in Aluminum Nanoparticle Arrays. *ACS Nano* **2013**, *7*, 5834−5841.

(27) Sugawara, A.; Mae, K. Surface Morphology of Epitaxial LiF(110) and CaF2(110) Layers. *J. Vac. Sci. Technol., B: Microelectron. Process. Phenom.* **2005**, *23*, 443−448.

(28) Intartaglia, R.; Das, G.; Bagga, K.; Gopalakrishnan, A.; Genovese, A.; Povia, M.; Di Fabrizio, E.; Cingolani, R.; Diaspro, A.; Brandi, F. Laser Synthesis of Ligand-Free Bimetallic Nanoparticles for Plasmonic Applications. *Phys. Chem. Chem. Phys.* **2013**, *15*, 3075−3082.

(29) Campaigne, E.; Meyer, W. W. Preparation and Absorption Spectra of p-Mercaptocinnamic and p-Mercaptobenzoic Acids and Derivatives. *J. Org. Chem.* **1962**, *27*, 2835−2841.

(30) Malinsky, M. D.; Kelly, K. L.; Schatz, G. C.; Van Duyne, R. P. Chain Length Dependence and Sensing Capabilities of the Localized Surface Plasmon Resonance of Silver Nanoparticles Chemically Modified with Alkanethiol Self-Assembled Monolayers. *J. Am. Chem. Soc.* **2001**, *123*, 1471−1482.

(31) Michota, A.; Bukowska, J. Surface-Enhanced Raman Scattering (SERS) of 4-Mercaptobenzoic Acid on Silver and Gold Substrates. *J. Raman Spectrosc.* **2003**, *34*, 21−25.

(32) Fazio, B.; D'Andrea, C.; Bonaccorso, F.; Irrera, A.; Calogero, G.; Vasi, C.; Gucciardi, P. G.; Allegrini, M.; Toma, A.; Chiappe, D.; Martella, C.; Buatier de Mongeot, F. Re-Radiation Enhancement in Polarized Surface-Enhanced Resonant Raman Scattering of Randomly Oriented Molecules on Self-Organized Gold Nanowires. *ACS Nano* **2011**, *5*, 5945−5956.

(33) Willets, K. A.; Van Duyne, R. P. Localized Surface Plasmon Resonance Spectroscopy and Sensing. *Annu. Rev. Phys. Chem.* **2007**, *58*, 267−297.

(34) Weiland, T. A. Discretization Method for the Solution of Maxwell's Equations for Six-Component Fields. *AEU Int. J. Electron. Commun.* **1977**, *31*, 116−120.

(35) Rakić, A. D.; Djurišić, A. B.; Elazar, J. M.; Majewski, M. L. Optical Properties of Metallic Films for Vertical-Cavity Optoelectronic Devices. *Appl. Opt.* **1998**, *37*, 5271−5283.

(36) Maya Girón, J. V.; Zelaya, E.; Rubert, A.; Benítez, G.; Carro, P.; Salvarezza, R. C.; Vela, M. E. Surface Chemistry of 4 - Mercaptobenzoic Acid Self-Assembled on Ag(111) and Ag Nano-particles. *J. Phys. Chem. C* **2013**, *117*, 24967−24974.

(37) Fleger, Y.; Mastai, Y.; Rosenbluh, M.; Dressler, D. H. Surface Enhanced Raman Spectroscopy of Aromatic Compounds. *Surf. Sci.* **2009**, *603*, 788−793.

(38) Wang, Y.; Ji, W.; Sui, H.; Kitahama, Y.; Ruan, W.; Ozaki, Y.; Zhao, B. Exploring the Effect of Intermolecular H-Bonding: A Study on Charge-Transfer Contribution to Surface-Enhanced Raman Scattering of p-Mercaptobenzoic Acid. *J. Phys. Chem. C* **2014**, *118*, 10191−10197.

(39) Gonella, G.; Cavalleri, O.; Terreni, S.; Cvetko, D.; Floreano, L.; Morgante, A.; Canepa, M.; Rolandi, R. High Resolution X-Ray Photoelectron Spectroscopy of 3-Mercaptopropionic Acid Self-Assembled Films. *Surf. Sci.* **2004**, *566−568*, 638−643.

(40) Bisio, F.; Proietti Zaccaria, R.; Moroni, R.; Maidecchi, G.; Alabastri, A.; Gonella, G.; Giglia, A.; Andolfi, L.; Nannarone, S.; Mattera, L.; Canepa, M. Pushing the High Energy Limit of Plasmonics. *ACS Nano* **2014**, *8*, 9239−9247.

(41) Alabastri, A.; Toma, A.; Liberale, C.; Chirumamilla, M.; Giugni, A.; De Angelis, F.; Das, G.; Di Fabrizio, E.; Zaccaria, R. P. Interplay Between Electric and Magnetic Effect in Adiabatic Polaritonic Systems. *Opt. Express* **2013**, *21*, 7538−7548.

(42) Maier, S. A.; Kik, P. G.; Atwater, H. A. Observation of Coupled Plasmon-Polariton Modes in Au Nanoparticle Chain Waveguides of Different Lengths: Estimation of Waveguide Loss. *Appl. Phys. Lett.* **2002**, *81*, 1714−1716.

(43) Necas, D.; Klapetek, P. Gwyddion: an Open-Source Software for SPM Data Analysis. *Cent. Eur. J. Phys.* **2012**, *10*, 181−188.